J Adv Ceram

Research Article

Robust and thermally insulating SiBCN/SiOC ceramic aerogel with superior electromagnetic wave absorption performance and high-temperature stability up to 1600 °C

Jiale Wang[1], Yifan Li[1], Jingrui Cao[1], Yixin Zhang[1], Boxuan Feng[1], Anran Guo[1], Liwen Yan[1,✉], Ping Hu[2,✉], Jiachen Liu[1]

Cite this article: Wang J, Li Y, Cao J, et al. *J Adv Ceram* 2026, **15**(3): 9221256. https://doi.org/10.26599/JAC.2026.9221256

ABSTRACT: SiBCN ceramic aerogels have emerged as a new generation of integrated thermal insulation and microwave absorption materials but face great challenges in terms of mechanical properties, high-temperature stability, and absorption bandwidth in practical applications. Herein, SiBCN/SiOC composite ceramic aerogels were prepared by solvent thermal crosslinking, freeze-drying, and pyrolysis of precursors. Polyhydromethylsiloxane (PHMS) was introduced *in situ* by the hydrosilane addition reaction during the solvothermal process, which endowed the precursor aerogel with a complex and robust three-dimensional network structure and further resulted in a 260% improvement in the compressive strength of the SiBCN/SiOC composite aerogel compared with that of the pure SiBCN aerogel. Additional investigations revealed that the SiBCN/SiOC composite aerogel enjoyed a low thermal conductivity (0.044–0.051 $W \cdot m^{-1} \cdot K^{-1}$) and a light weight (0.13–0.16 $g \cdot cm^{-3}$), which was favorable for thermal barrier material. Notably, the SiBCN/SiOC composite aerogel exhibited excellent microwave absorption performance with an effective absorption bandwidth of 6.7 GHz and a reflection loss of −43.89 dB at a thickness of 2.5 mm due to improved impedance matching, multiple reflections, and enhanced interfacial polarization. Furthermore, the introduction of SiOC significantly inhibited the crystallization of SiBCN at high temperatures. After heat treatment at 1600 °C, the composite aerogel retained its amorphous nanoparticle pearl-chain-like structure, with thermal conductivity remaining as low as 0.052 $W \cdot m^{-1} \cdot K^{-1}$. The *in situ* introduction of PHMS provided novel insight and a promising strategy for enhancing the overall performance of SiBCN ceramic aerogels, expanding their application in high-temperature environments.

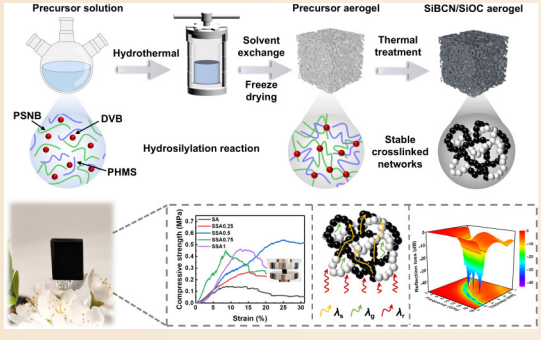

KEYWORDS: SiBCN/SiOC ceramic aerogel; thermal insulation; electromagnetic wave absorption; high-temperature stability

1 Introduction

The development of hypersonic vehicles, facilitated by progress in aerospace technology, has created an urgent need for multifunctional thermal insulation materials, such as thermal insulation and electromagnetic wave (EMW) absorption integrated materials [1]. Ceramic aerogels [2], as high-temperature insulating materials with a nanoscale three-dimensional porous network structure, show significant application prospects in extreme environmental thermal protection systems due to their low density, high-temperature resistance, and low thermal conductivity [3–5]. Although conventional oxide ceramic aerogels exhibit low density and ultralow thermal conductivity [6–8], they tend to undergo phase transformation, crystallization, and sintering at elevated temperatures [9]. These factors lead to structural collapse and a significant decline in thermal insulation performance [10]. Meanwhile, carbon aerogels are highly susceptible to oxidation and are oxidized in an oxygen-containing environment above 400 °C [11]. Consequently, recent research has increasingly focused on non-oxide ceramic aerogels such as SiC [12,13], Si_3N_4 [14–16], SiCN [17,18], and SiBCN [19–21]. Non-oxide ceramic aerogels demonstrate favorable properties, including low density, low thermal conductivity, and excellent ultrahigh temperature stability, making them suitable for thermal protection applications at temperatures over 1600 °C [22]. Among these non-oxide ceramic aerogels, the SiBCN ceramic aerogel derived from polyborosilane (PSNB) precursors exhibits lower density (0.042–0.22 $g \cdot cm^{-3}$), higher specific surface area (66.2–850 $m^2 \cdot g^{-1}$), and lower thermal conductivity (0.025–

[1] Key Laboratory of Advanced Ceramics and Machining Technology of Ministry of Education, Tianjin University, Tianjin 300072, China. [2] National Key Laboratory of Science and Technology on Advanced Composites in Special Environments, Harbin Institute of Technology, Harbin 150080, China.

✉ Corresponding authors. E-mail: L. Yan, lwyan@tju.edu.cn; P. Hu, huping@hit.edu.cn

Received: November 19, 2025; Revised: January 29, 2026; Accepted: January 31, 2026

0.082 $W \cdot m^{-1} \cdot K^{-1}$) owing to their ultrahigh porosity and unique nanoporous structure and is expected to be used as a high-temperature insulating material above 1600 °C [23,24].

Unlike SiBCN dense ceramics [25], the preparation of SiBCN ceramic aerogels requires the introduction of divinylbenzene (DVB) as a crosslinking agent to form a stable gel structure [26]. However, this approach results in an excessively high content of free carbon within the SiBCN aerogel [27]. At elevated temperatures, the excessive free carbon makes SiC crystals more prone to precipitation [28], leading to the destruction of the aerogel skeleton. As a result, the high-temperature structural stability of the SiBCN aerogel was severely affected. Meanwhile, a strong correlation has been established between SiBCN ceramic aerogel and its organic precursor gel in terms of structural characteristics and mechanical properties. The limited number of silicon hydrogenation reaction sites in PSNB results in a low degree of solvent thermal crosslinking, which in turn leads to the relatively weak mechanical strength of the SiBCN aerogel nanoskeleton [29]. Therefore, appropriate strategies should be implemented to enhance the crosslinking degree of the gel network while simultaneously reducing the free carbon content. Polyhydromethylsiloxane (PHMS) contains more silane reaction sites than PSNB. These groups exhibit higher reactivity, promoting a wider range of solvent thermal crosslinking [30]. Meanwhile, the *in situ* introduction of SiOC can enhance interfacial polarization and optimize impedance matching, thereby improving the EMW absorption performance of SiBCN ceramic aerogels [31,32]. In addition, during the high-temperature thermal treatment process, oxygen in SiOC will react with free carbon, which inhibits the crystallization of amorphous SiBCN. Therefore, the synthesis of SiBCN/SiOC composite ceramic aerogels is expected to achieve a synergistic improvement in the EMW absorption performance, high-temperature stability, and mechanical strength of SiBCN-based aerogels while maintaining their inherent advantages, such as low density and low thermal conductivity.

Here, to improve the mechanical strength and EMW absorption capacity of SiBCN ceramic aerogels, as well as address the issue of high-temperature crystallization and improve the thermal stability, SiBCN/SiOC composite ceramic aerogels were synthesized through solvothermal synthesis, freeze-drying, and thermal treatment processes. The morphology and properties of the SiBCN/SiOC ceramic aerogel were regulated by adjusting the SiOC content via variation of the initial PSNB to PHMS ratio. As a result, the compressive strength of the SiBCN/SiOC ceramic aerogel significantly increased by 260%, with the specific strength rising from 1256 to 3756 $N \cdot m \cdot kg^{-1}$. The EMW absorption performance of the ceramic aerogel was also significantly improved after the introduction of SiOC, with the optimal reflection loss (RL) reaching −55.39 dB and the effective absorption bandwidth (EAB) expanding to 6.7 GHz. Furthermore, the composite aerogel exhibited excellent structural stability at temperatures up to 1600 °C under an inert atmosphere. This study offers valuable insights into the development of multifunctional ceramic aerogels that combine low density, excellent EMW absorption performance, high mechanical strength, superior high-temperature structural stability, and outstanding thermal insulation performance.

2 Experimental methods

2.1 Materials

PSNB was supplied by the Institute of Chemistry, Chinese Academy of Sciences. PHMS was obtained from Shanghai Macklin Biochemical Technology Co., Ltd. DVB was obtained from Shanghai Aladdin Biochemical Technology Co., Ltd. Hexane, cyclohexane, and xylene were obtained from Tianjin Kermel Chemical Reagent Co., Ltd. Karstedt catalyst solution (2 wt% Pt) was obtained from Rhawn Chemical Reagent Co., Ltd. The Pt catalyst was diluted in xylene prior to use with a platinum content of 0.1 wt%. All the chemicals were analytical-grade and used as received.

2.2 Preparation of SiBCN/SiOC ceramic aerogels

The precursor solution was obtained by dissolving PSNB and PHMS in hexane (90 vol%) and stirring for 20 min with mass ratios of SiBCN to SiOC of 1 : 0.25, 1 : 0.5, 1 : 0.75, and 1 : 1. The corresponding samples were labeled SSA0.25, SSA0.5, SSA0.75, and SSA1. The amount of DVB added was equal to the total weight of the PSNB and PHMS. Subsequently, 200 μL of Pt catalyst solution (0.1 wt%) was added, followed by stirring for 15 min. The homogeneous solution was then transferred into a hydrothermal vessel (200 mL) and heated in an oven at 160 °C for 20 h. Upon cooling, the wet gels were transferred into beakers filled with cyclohexane, and solvent exchange was performed once daily for 2–3 d. Thereafter, the wet gels were freeze-dried at −50 °C for 48 h to produce the precursor xerogel. Finally, SiBCN/SiOC composite ceramic aerogels (SSAs) were formed by thermal treatment at 1200 °C for 2 h under a flowing argon atmosphere. In addition, pure SiBCN aerogels (SAs) were prepared using only PSNB for comparison. The preparation process of SAs was basically the same as that of SSAs except that no PHMS was added.

2.3 Characterization methods

The densities of the SSA and SA were calculated according to the mass and dimension of the samples. The chemical structures of the preceramic aerogels and SSAs were characterized by a Fourier transform infrared spectrometer (FT-IR; Nicolet instrument, USA). The morphology of the aerogel was observed by a scanning electron microscope (SEM; TDCLS-S4800, Japan). The pore structures of the aerogel samples were obtained by using a nitrogen adsorption–desorption analyzer (ASAP 2460 aperture analyzer, Micromeritics, USA). The chemical states of the aerogel samples were analyzed using an X-ray photoelectron spectrometer (XPS; ESCALAB-Xi, Thermo Fisher, USA). The thermal conductivity of the SA and SSA at room temperature was investigated by the hot-disk method using a thermal constant analyzer (TPS2500S, Hot Disk, Sweden) on samples with dimensions of 10 mm × 10 mm × 20 mm. The compressive strength of SAs and SSAs was investigated using an electronic universal testing machine (LD24.204, Lishi (Shanghai) Scientific Instruments Co., Ltd, China) on samples with dimensions of 10 mm × 10 mm × 12 mm. The relative complex permeability and permittivity of the aerogels were gauged through a vector network analyzer (N5234A, Agilent Technologies Inc., USA) using the coaxial line method. For sample preparation, the aerogels were evenly mixed with paraffin wax at an 80% weight proportion of paraffin and formed into a ring with an inner diameter of 3 mm and an outer diameter of 7 mm. According to the transmission line theory, the reflection loss of the material can be calculated based on the measured data of the relative complex permeability and permittivity. To investigate the effect of siloxane incorporation on the high-temperature thermal stability of composite aerogels, the obtained SSA0.5 sample was annealed at 1600 °C in argon for 60 min, and the microstructure,

composition, and thermal conductivity of the heat-treated sample were further characterized.

3 Results and discussion

As illustrated in Fig. 1, SSAs were prepared from PSNB, PHMS, and DVB through solvothermal and freeze-drying, followed by pyrolysis. The content of SiOC in SSAs could be effectively regulated by changing the initial ratio of PSNB and PHMS. The formation of the precursor gel network, namely, gelation, was fundamentally attributed to the hydrosilylation reaction [21]. During the solvothermal process, Si–H bonds in polymethylhydrosiloxane and polyborosilazane reacted with the C=C bonds from the crosslinking agent divinylbenzene, as shown in Fig. 2, to form a stable three-dimensional gel network connected by Si–C bonds [30,33]. The reaction chemically bonded the two precursors at the molecular scale and *in situ* transformed them into a nanoparticle composite ceramic aerogel with an amorphous phase after the subsequent 1200 °C pyrolysis process. Due to the presence of a large amount of unreacted organic solvents in the wet gel and the freezing point of n-hexane being −95 °C, solvent replacement was necessary [34]. Here, cyclohexane with a higher freezing point was used instead of hexane in the wet gel, and then freeze-drying was carried out. Finally, SSAs were obtained after heat treatment at 1200 °C for 2 h in a flowing argon atmosphere.

The chemical structures of the composite aerogels were characterized by FT-IR spectroscopy, and the results are shown in Figs. 3(a) and 3(b). The FT-IR spectra of all the precursor aerogels of SSAs are shown in Fig. 3(a). The absorption peaks at 1080 and 1260 cm^{-1} were assigned to the Si–O–Si and Si–CH_3 groups of PHMS. The absorption peak centered at 1602 cm^{-1} was ascribed to the stretching vibrations of C=C bonds in DVB. The band between 1350 and 1450 cm^{-1} was attributed to the B–N bonds in PSNB, while the peak at 2920 cm^{-1} originated from the C–H bonds in both DVB and PHMS. The absorption peak at 2150 cm^{-1}

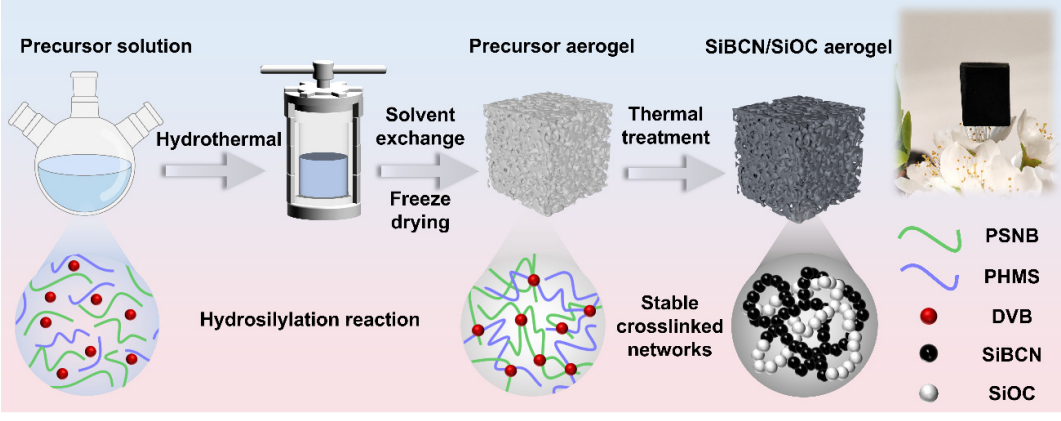

Fig. 1 Schematic diagram of preparation process of SiBCN/SiOC ceramic aerogel.

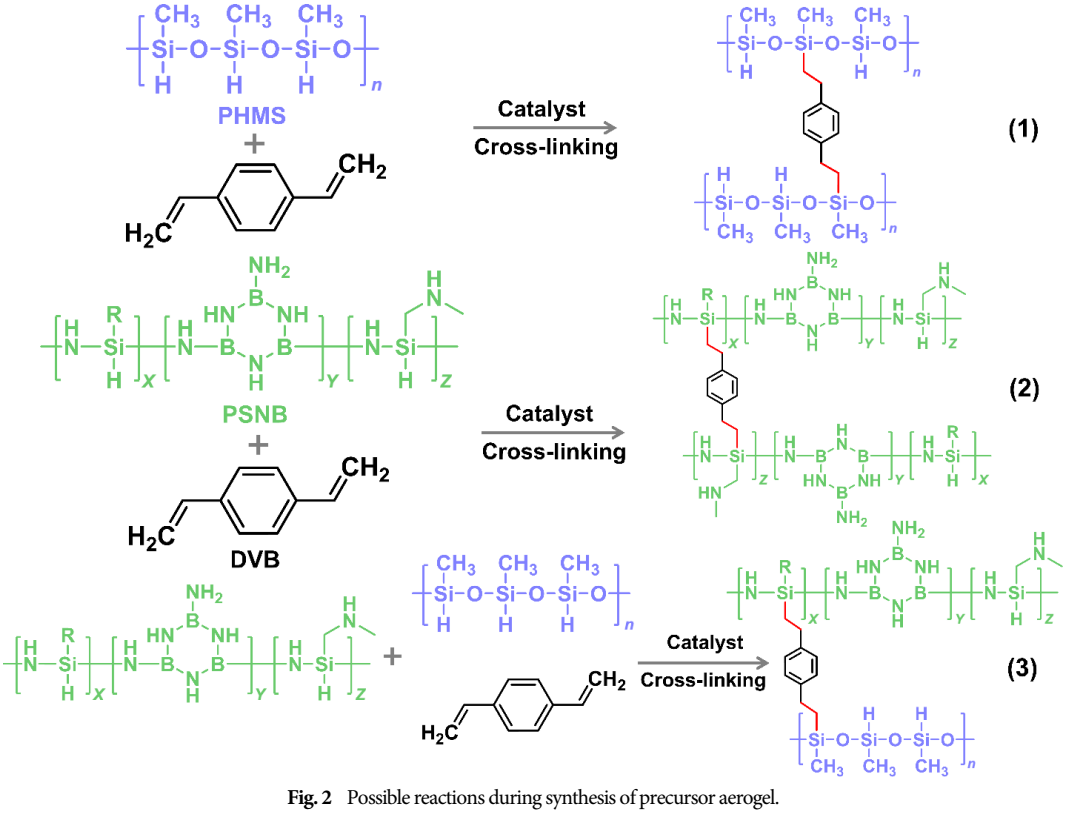

Fig. 2 Possible reactions during synthesis of precursor aerogel.

清華大学出版社 Tsinghua University Press | SciOpen

was attributed to the stretching vibration of the –Si–H bonds in PHMS and PSNB. Meanwhile, the absorption peak at 1049 cm^{-1} was caused by the vibration of the Si–CH_2CH_2– bonds formed by the reaction of the Si–H groups of PSNB and PHMS with the –CH=CH_2 groups of DVB, proving that the hydrosilane addition reaction occurred [21,30]. The infrared spectra of the composite ceramic aerogels after heat treatment are shown in Fig. 3(b). Compared with Fig. 3(a), the vibration peaks of –CH_3 bonds and –Si–H bonds completely disappeared. Furthermore, the original peak of the Si–O–Si bonds at 1045 cm^{-1} became strong and wide, and a weak peak belonging to the Si–C bonds appeared at 584 cm^{-1}. These phenomena indicated the transformation of the aerogel from an organic structure to an inorganic structure [35]. The absorption peak centered at 1630 cm^{-1} was attributed to the tensile vibration of the C=C bonds in free carbon. The absorption peak that occurred at 1384 cm^{-1} was caused by the stretching vibration of the B–N bonds. The formation of Si–O–Si bonds and Si–C bonds was conducive to improving the thermal stability of the composite ceramic aerogels. The XRD patterns of all SSA samples are shown in Fig. 3(c). Obvious broad and diffuse scattering peaks could be observed, which indicated that the aerogels synthesized at 1200 °C were all amorphous. The ceramic yield of the composite aerogels increased from 45.86% for SSA0.25 to 51.94% for SSA1. The reason was that the ceramic yield of PHMS was higher than that of PSNB [30]. Combining the XRD patterns and FT-IR spectra, it could be inferred that the SSA was mainly composed of uniformly distributed SiBCN and SiOC amorphous nanophases.

The microstructure images of SAs and SSAs are shown in Figs. 3(d)–3(i). The results showed that when PHMS was added, the particle size of the aerogel was smaller than that of the SA, and the microscopic three-dimensional network structure was more stable. The elemental mapping images revealed the uniform distribution of Si, C, O, N, and B in SSA0.5, as illustrated in Fig. S1 in the Electronic Supplementary Material (ESM), indicating the homogeneous dispersion of SiOC within the SSA. To further explore the pore structure features of the aerogels, the N_2 adsorption–desorption behavior of all samples was evaluated. Figures 4(a) and 4(b) illustrate the hysteresis loops and pore size distributions of all the samples. According to the IUPAC classification, all curves showed type IV isotherms with H3 hysteresis loops (Fig. 4(a)). These results meant that all samples presented similar pore structures. The hysteresis loops of capillary condensation at high relative pressure indicated that the synthesized aerogels contained macropores in addition to mesopores [21]. These results were consistent with the SEM observation results. Therefore, as shown in Fig. 4(b), all aerogel samples had a hierarchical porous structure with pore diameters mostly ranging between 10 and 70 nm. The corresponding pore structure parameters of all samples are listed in Table 1. The average aperture of SSA0.5 was the smallest by comparison. It should be mentioned that with increasing SiOC content, the Brunauer–Emmett–Teller (BET) surface area showed a gradually increasing trend [30]. Compared with the SA, the BET surface area of SSA0.5 increased from 56.39 to 116.18 $m^2 \cdot g^{-1}$. The improvement was attributed to the introduction of PHMS, which partially replaced PSNB in the solvothermal crosslinking process. Moreover, the molecular chains of PHMS contained a higher

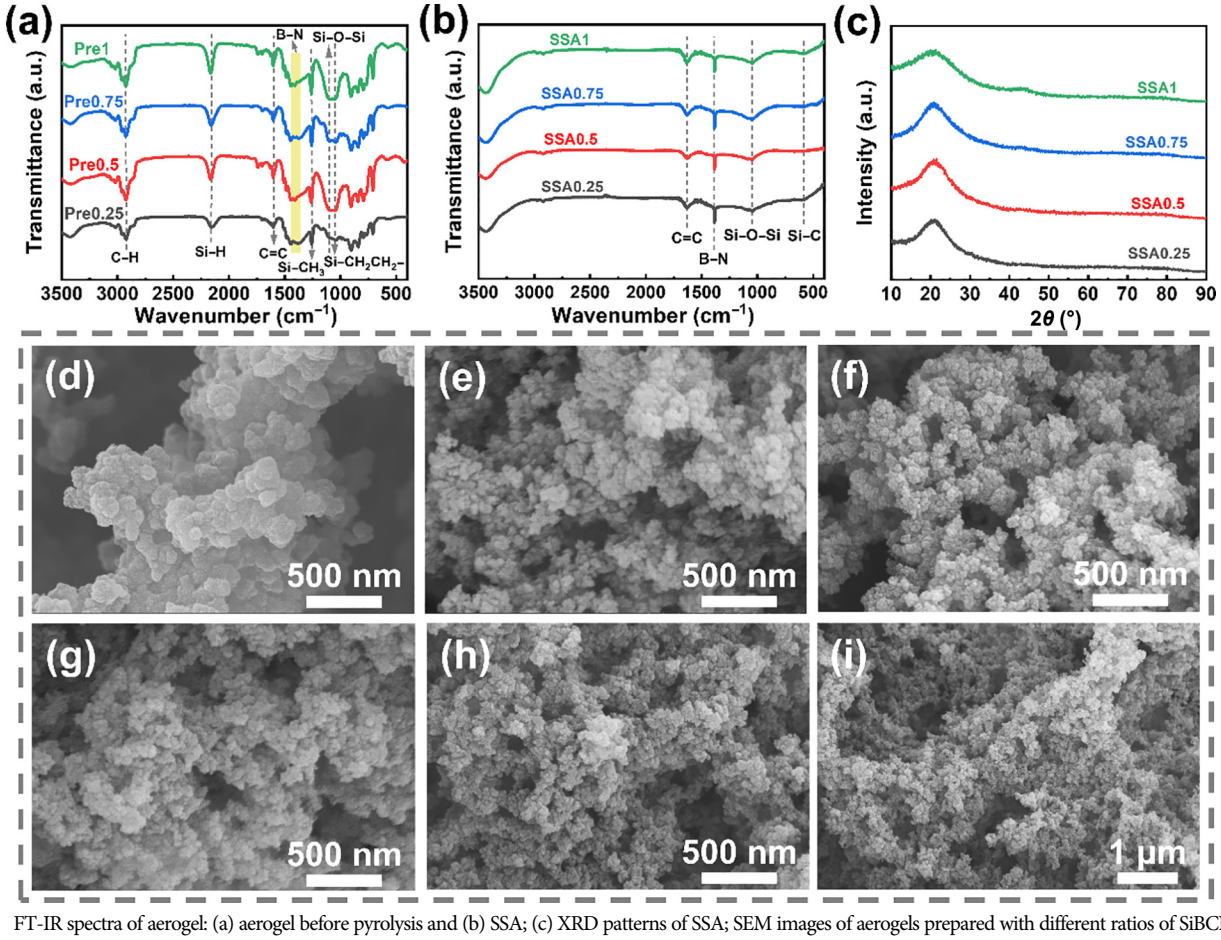

Fig. 3 FT-IR spectra of aerogel: (a) aerogel before pyrolysis and (b) SSA; (c) XRD patterns of SSA; SEM images of aerogels prepared with different ratios of SiBCN and SiOC: (d) SA, (e) SSA0.25, (f) SSA0.5, (g) SSA0.75, and (h, i) SSA1.

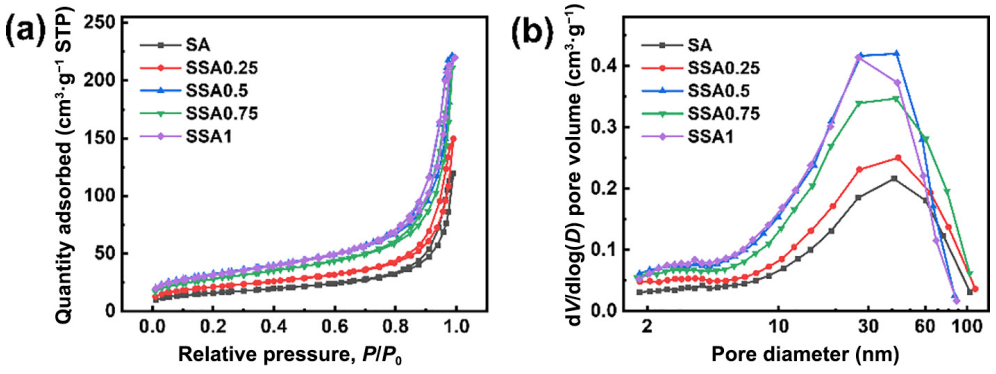

Fig. 4 (a, b) Nitrogen adsorption–desorption curves and pore size distributions of aerogel samples.

Table 1 Pore structure features of aerogel samples

Sample	BET surface area ($m^2 \cdot g^{-1}$)	Pore volume ($cm^3 \cdot g^{-1}$)	Average pore diameter (nm)
SA	56.39	0.185	13.13
SSA0.25	75.09	0.231	12.31
SSA0.5	116.18	0.343	11.81
SSA0.75	100.62	0.326	12.96
SSA1	112.15	0.334	12.04

density of Si–H bonds than those in PSNB, leading to a more robust and extensive crosslinked network. A better degree of solvent-thermal crosslinking could be obtained. The aerogel skeleton particles with a three-dimensional nanonetwork structure were uniformly dispersed, thereby making the microstructure distribution of SSAs more uniform. The TEM characterization showed that the aerogel particles consist of an amorphous SiBCN/SiOC nanophase and free carbon (Fig. 5). The aerogel particles displayed typical amorphous traits, as indicated by the selected area electron diffraction (SAED) pattern inset in Fig. 5(b). At the same time, compared with the TEM image of the SA (Fig. S2 in the ESM), it was found that there were more heterogeneous interfaces in the SSA0.5 sample. As a result of the *in situ* introduced SiOC, multiple heterogeneous interfaces among amorphous SiBCN, free carbon, and amorphous SiOC were constructed, which augmented the interface and dielectric polarization loss and consequently enhanced the EMW absorption performance [32,36].

To clarify the shrinkage behavior of aerogels during the organic–inorganic transformation, the linear shrinkage rates of various aerogels before and after pyrolysis at 1200 °C were measured, as shown in Fig. 6(a). The results indicated that the average linear shrinkage rates of all samples after heat treatment were approximately 32%, with no significant variation observed.

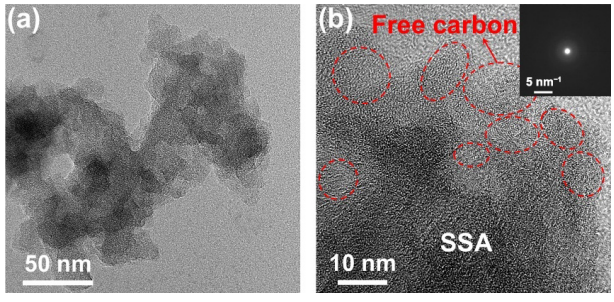

Fig. 5 (a, b) TEM and SAED images of SiBCN/SiOC aerogel (SSA0.5).

The incorporation of SiOC was found to have a negligible effect on the shrinkage behavior of the aerogels under high-temperature pyrolysis. The density of the aerogels showed a slight increasing trend, rising from 0.12 to 0.16 $g \cdot cm^{-3}$ with increasing SiOC content, as shown in Fig. 6(b). Under the condition of constant linear shrinkage, the rise in ceramic yield led to an increase in mass per unit volume, thereby resulting in higher density. Despite the modest density increase, SSA0.5 can still be readily positioned on the top of a stamen, as demonstrated in Fig. 1. The compressive strengths of SSAs and SAs are shown in Fig. 6(b). The introduction of SiOC increased the compressive strength of the aerogel from 0.147 to 0.507 MPa. The compressive stress–strain curves of all the samples are shown in Fig. 6(c). From the results, the compressive strength of all the samples increased to the maximum value with increasing strain and then dropped sharply, indicating the brittleness of the ceramic aerogels. With the increase in the SiOC ratio, the compressive strength of SSAs gradually increased and then decreased, reaching the maximum value of 0.507 MPa at SSA0.5. The introduction of SiOC effectively enhanced the mechanical strength of the SiBCN ceramic aerogel. From the perspective of chemical reactions, the addition of PHMS made the composite gel network structure

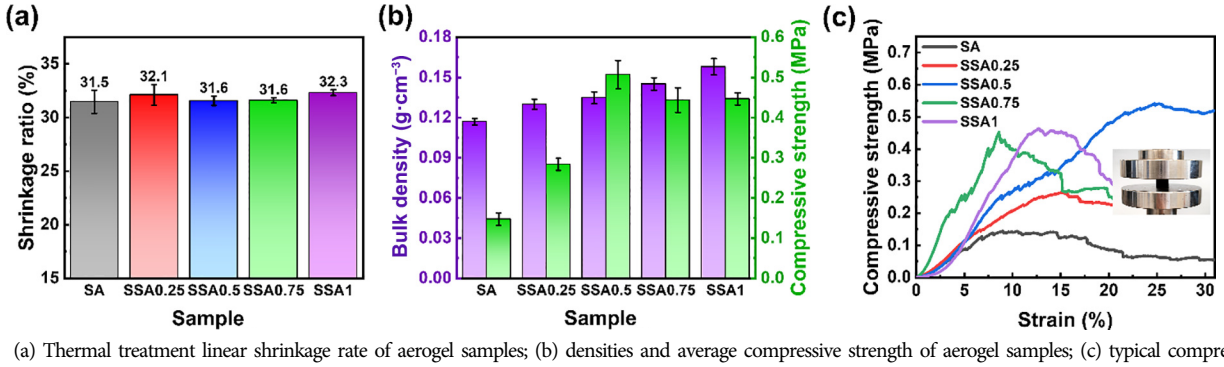

Fig. 6 (a) Thermal treatment linear shrinkage rate of aerogel samples; (b) densities and average compressive strength of aerogel samples; (c) typical compression stress–strain curves of aerogel samples.

清華大学出版社 Tsinghua University Press | SciOpen

more stable. A tighter network structure at the molecular scale enhanced the mechanical properties of the aerogels [37,38]. On the other hand, the ceramic yield of SiOC was higher than that of SiBCN [30], so the increase in solid content also enhanced the compressive strength of SSAs. Additionally, from Fig. 3(f), the network structure of SSA0.5 was more complex. The three-dimensional networks of nanoparticles supported each other, which improved the mechanical properties of the SSA0.5 sample.

The thermal conductivity of the material is a critical property for thermal insulation in aircraft applications, serving as a key parameter in determining its practical viability. As shown in Fig. 7(a), a fresh flower was directly placed on an aluminum plate heated by the flame of an alcohol burner. After being heated for 90 s, the flower was severely charred. To prove the heat insulation performance of the SSA, SSA0.5 was placed between the aluminum plate and the flower as an example. Despite being heated for 90 s, the flower remained intact (Fig. 7(b)). The results indicated that SSAs exhibited excellent thermal insulation performance and showed great potential for thermal insulation applications. The thermal infrared images of SSA0.5 on the heated aluminum plate of the alcohol burner are shown in Fig. 7(c). After heating for 90 s, the top surface of SSA0.5 remained at room temperature, while heat continued to accumulate at the bottom. Meanwhile, as shown in Fig. 7(d), the thermal conductivity of the SA was 0.0441 $W \cdot m^{-1} \cdot K^{-1}$. With increasing SiOC content, the thermal conductivity of the composite ceramic aerogels exhibited a slight increase. When the ratio of SiBCN to SiOC was 1 : 0.5, the thermal conductivity of the composite aerogel was 0.0458 $W \cdot m^{-1} \cdot K^{-1}$. Compared with SAs, the thermal conductivity of SSAs increased by only 0.0017 $W \cdot m^{-1} \cdot K^{-1}$, while the compressive strength was increased by 264%. On the premise of maintaining the inherent heat insulation performance of granular aerogel, the

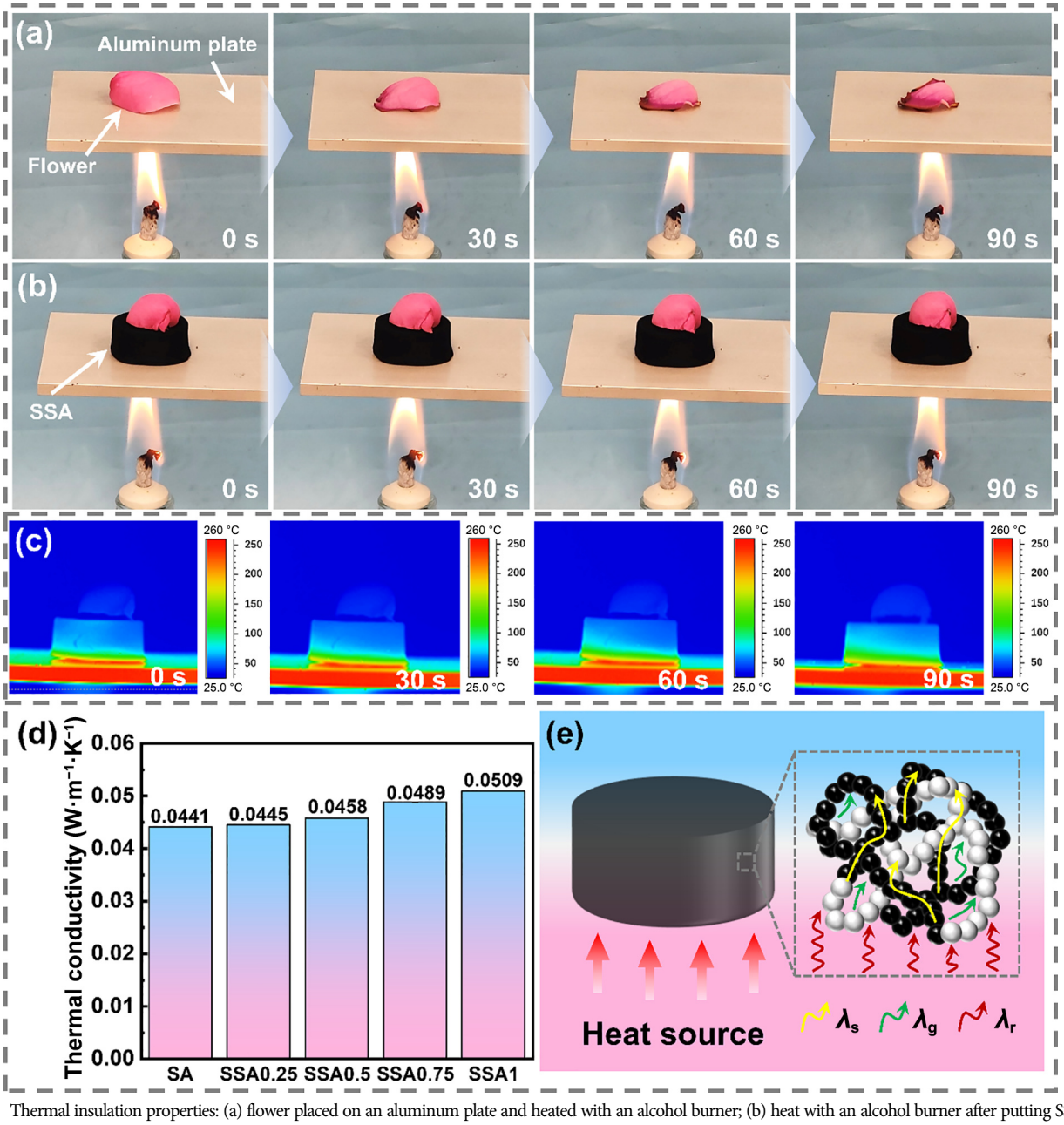

Fig. 7 Thermal insulation properties: (a) flower placed on an aluminum plate and heated with an alcohol burner; (b) heat with an alcohol burner after putting SSA0.5 between the flower and aluminum plate; (c) thermographic images of SSA0.5 during heating with an alcohol burner; (d) thermal conductivity of aerogel samples; (e) thermal transport pathways inside SSAs.

mechanical properties of the composite aerogel were significantly improved. Based on the above analysis, it was necessary to control the content of the introduced SiOC to achieve the comprehensive performance required by SSAs in practical applications.

A schematic diagram of the heat transfer mechanism of the SSA is shown in Fig. 7(e). The effective total thermal conductivity (λ_t) can be expressed as the sum of the radiant thermal conductivity (λ_r), the gas thermal conductivity (λ_g), and the solid thermal conductivity (λ_s) by Eq. (1) [39,40]:

$$\lambda_t = \lambda_r + \lambda_g + \lambda_s \quad (1)$$

The radiant thermal conductivity was very weak at room temperature and could be ignored. Therefore, the λ_t of SSAs was mainly determined by λ_g and λ_s. As mentioned above, the average pore size of SSAs was mainly distributed within the range of 10–60 nm. The pore size of SSAs was relatively small compared with the average free path of gas molecules in air (approximately 70 nm). Because the characteristics of this pore structure greatly reduced the collision probability between gas molecules, λ_g was significantly inhibited [41]. λ_s was mainly caused by phonon transfer, and the main influencing factors of λ_s were solid composition and volume density. The numerous interfaces within SSAs had an inhibitory effect on phonon transfer and led to an aerogel with a low λ_s [42]. Furthermore, the "infinitely long path effect" caused by the 3D nanonetwork structure of SSAs significantly reduced λ_s. As a result, SSAs exhibited low λ_t and excellent adiabatic properties. Overall, the outstanding heat insulation performance of SSAs made ceramic aerogels promising for application in extreme environments.

To measure the electromagnetic wave absorbing capability, the prepared aerogels were uniformly blended with paraffin to fabricate circular samples with inner and outer diameters of 3 and 7 mm, respectively. The microwave dissipation performance is characterized by RL, which is calculated using Eqs. (2) and (3) [43]:

$$Z_{in} = \sqrt{\frac{\mu_r}{\varepsilon_r}} \tanh\left(j\frac{2\pi f d}{c}\sqrt{\mu_r \varepsilon_r}\right) \quad (2)$$

$$RL = 20\log\left|\frac{Z_{in} - 1}{Z_{in} + 1}\right| \quad (3)$$

where Z_{in} denotes the input impedance of the absorber, ε_r and μ_r represent the relative complex permittivity and permeability, f indicates the frequency of the incident wave, c is the velocity of microwave propagation, and d refers to the thickness of the material. It is important to note that lower RL values indicate superior EMW absorption performance. Specifically, when the RL is below −10 dB, over 90% of the incident EMW can be attenuated, and the corresponding frequency range can be referred to as the EAB [44].

The RL curves of SA and SSA samples with varying thicknesses are summarized in Fig. 8(a). It was apparent that all aerogel samples exhibit excellent microwave absorption performance within specific frequency ranges at certain thicknesses. In detail, the RL_{min} value of SA was just −31.75 dB with a matching thickness of 7.3 mm. The RL_{min} values of SSA0.25, SSA0.5, SSA0.75, and SSA1 reached −46.85, −45.74, −55.39, and −50.52 dB, corresponding to thicknesses of 9.6, 2.9, 8.1, and 7.2 mm, respectively. From the results, the RL_{min} value of SSAs was significantly lower than that of SAs, and the minimum RL_{min} value was reduced to −55.39 dB. Meanwhile, we evaluated the reflection loss of all samples within the thinner thickness range of 1–5 mm (Fig. S3 in the ESM) and found that the SSA0.5 sample exhibited superior electromagnetic wave absorption performance. The enhancement can be primarily attributed to the graphitization of free carbon and the incorporation of an appropriate amount of SiOC phase. The multiphase components and microporous–mesoporous multilevel pore structure in SSA0.5 enhanced the interfacial polarization and promoted multiple scattering of electromagnetic waves, thereby significantly improving the dielectric loss capability of the composite aerogel [45].

As is well known, the electromagnetic parameters of materials are crucial to their microwave absorption capability [46]. To reveal the EMW absorption mechanism in detail, the electromagnetic parameters of SAs and SSAs were systematically investigated. Generally, the EMW absorption capability is primarily affected by ε_r ($\varepsilon_r = \varepsilon' - j\varepsilon''$) and μ_r ($\mu_r = \mu' - j\mu''$) [21,47]. Given that SAs and SSAs exhibit negligible magnetic properties, only dielectric loss was considered in this study. The ε' and ε'' for SAs and SSAs across different frequencies are illustrated in Figs. 8(b) and 8(c). It was evident that both the ε' and ε'' values of all samples decreased with increasing frequency, which was a typical manifestation of frequency dispersion [48]. Among all the ε' values of the samples, it was striking that the ε' of SSA0.5 increased to 9.68–4.64. For ε'', the values of SSA0.5 increased to 5.97–2.22. It has been widely recognized that ε' and ε'' refer to the storage and attenuation capabilities of EMW. Compared with the pure SiBCN aerogel, the *in situ* introduction of SiOC created abundant heterogeneous interfaces among SiBCN, SiOC, and free carbon, significantly enhanced interfacial polarization and thus elevated both the real and imaginary parts of the permittivity. In the SSA0.5 sample, the three phases were uniformly dispersed, which maximized the heterogeneous interface area and thereby led to pronounced interfacial polarization and increased permittivity.

From Figs. 8(b) and 8(c), both the ε′ line and the ε″ line show an obvious fluctuation as the frequency increases from 2 to 18 GHz. This was primarily attributed to the different relaxation times of various polarization mechanisms within the composite aerogel. Different polarizations were successively activated or reached their peak at different frequency bands, resulting in fluctuations in the complex permittivity of the samples. In the electromagnetic field, the dipole polarization resulting from the reorientation of polar bonds (such as Si–O, Si–N, and Si–C, etc.) and structural defects (e.g., dangling bonds) in composite aerogels gives rise to loss peaks at different frequencies. Significant variations in the dielectric constant at different frequencies could be induced by various types of interfacial polarization, including that at the interface between graphitic carbon and the amorphous matrix, between neighboring nanoparticles, and between nanoparticles and pores within the composite aerogel. Moreover, the combination of conductive loss from the graphitic carbon network and the aforementioned relaxation mechanisms led to more pronounced frequency-dependent fluctuations in the dielectric constant. The enhanced interfacial polarization and multiple reflection effects, facilitated by the appropriate dielectric constant and the *in situ* incorporation of SiOC, contribute to the superior EMW absorption performance of SSA0.5. Figure 8(d) displays the dielectric loss tangent ($\tan\delta_\varepsilon = \varepsilon''/\varepsilon'$) of the SA and SSA samples. Several distinct resonance peaks were observed, which should be attributed to dipole polarization phenomena [48].

The detailed polarization loss of SAs and SSAs during microwave energy loss was further investigated through the analysis of Cole–Cole semicircular patterns (Figs. 8(e)–8(i)). Based on the Debye theory, each semicircle represents a relaxation process and can be expressed as Eq. (4) [49,50]:

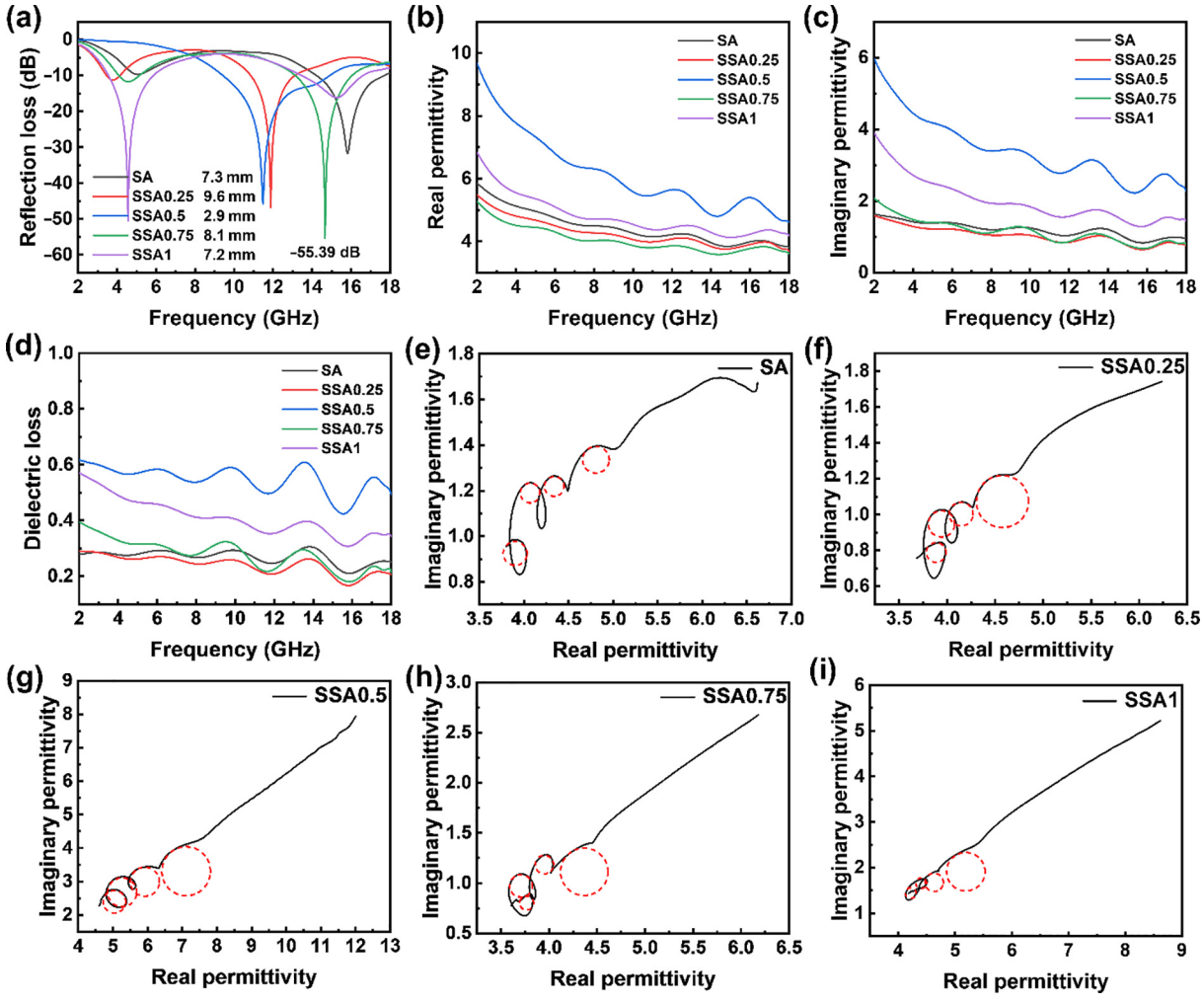

Fig. 8 (a) RL of all aerogel samples with varying thickness; complex permittivity of all aerogel samples: (b) real part and (c) imaginary part; (d) dielectric loss; Cole–Cole semicircle curves of all samples: (e) SA, (f) SSA0.25, (g) SSA0.5, (h) SSA0.75, and (i) SSA1.

$$\left(\varepsilon' - \frac{\varepsilon_s + \varepsilon_\infty}{2}\right)^2 + (\varepsilon'')^2 = \left(\frac{\varepsilon_s - \varepsilon_\infty}{2}\right)^2 \quad (4)$$

where ε_∞ and ε_s denote the dielectric constant at infinite frequency and the static dielectric constant, respectively. The Cole–Cole curves of all samples showed multiple semicircular curves, which reflected the complexity of the polarization relaxation mechanism within the aerogel material and indicated that there were multiple Debye relaxation processes within the aerogels. Both the SA and SSA samples contained the coexistence of interfacial polarization relaxation and dipole polarization relaxation, which led to the formation of the Cole–Cole semicircle. This phenomenon could be attributed to the gradual enhancement of interfacial polarization resulting from the numerous heterogeneous interfaces in SSAs and the dipole polarization induced by internal defects with the *in situ* introduction of SiOC [51].

The attenuation constant (α) and impedance matching coefficient (Z) of the absorbers are two critical elements influencing the microwave absorption performance of aerogel materials [52]. The impedance matching characteristics reflect the relationship between the input impedance and the free space impedance, which can be calculated by $Z = |Z_{in}/Z_0|$. When Z_{in} is equal to or close to Z_0, it indicates that more EMW energy is able to enter the absorber, while the reflection value from the surface is almost zero [32]. The α value reflects the EMW energy attenuation ability, which can be calculated by Eq. (5) [21]:

$$\alpha = \frac{\sqrt{2}\pi f}{c}\sqrt{\mu''\varepsilon'' - \mu'\varepsilon' + \sqrt{(\mu''\varepsilon'' - \mu'\varepsilon')^2 + (\mu'\varepsilon'' + \mu''\varepsilon')^2}} \quad (5)$$

The calculated α values of the SA and SSA at various frequencies are presented in Fig. 9(a). The results showed that the α values of both SAs and SSAs increased across the tested frequency range, suggesting that the absorber exhibited enhanced EMW attenuation performance at higher frequencies. Notably, the α values of all SSA samples have steadily increased, and the α value of SSA0.5 has the largest increase, reaching a maximum value of 205.8. Figure 9(b) illustrates the calculated Z values for all samples. The greater the difference between the Z value and 1, the worse the impedance matching of the absorbing material was. Remarkably, the Z value of the SSA0.5 sample approaches 1, which indicated that appropriate regulation of the content of SiOC in SSAs could substantially improve the impedance matching characteristics of the SSA. It was the optimized impedance matching that enabled SSA0.5 to exhibit stronger EMW absorption capability, which was consistent with the actual tested EMW absorption results described above.

As illustrated in Fig. 10(a), SSA0.5 exhibited an RL_{min} of –45.74 dB and an EAB of 6.7 GHz with a thickness of 2.5 mm. The EAB of the sample can cover the entire Ku band. The relationships among the RL_{min}, EAB, and sample thickness of SSA0.5 are shown in Figs. 10(b) and 10(c). SSA0.5 mainly consisted of an amorphous SiBCN matrix, *in situ* introduced

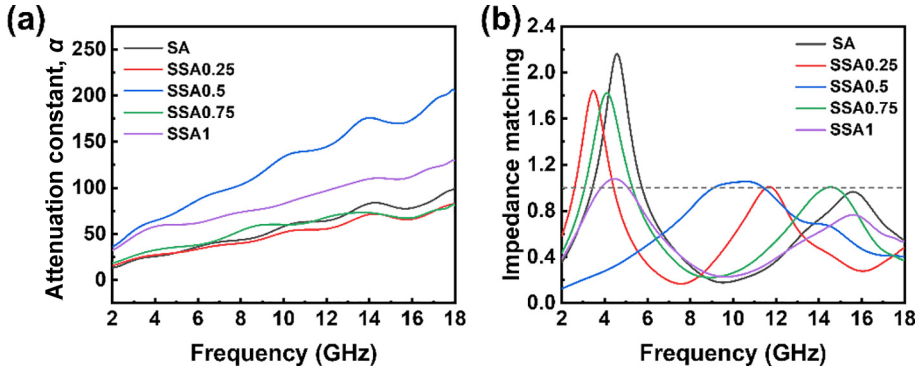

Fig. 9 (a) Attenuation constant and (b) impedance matching of all aerogel samples.

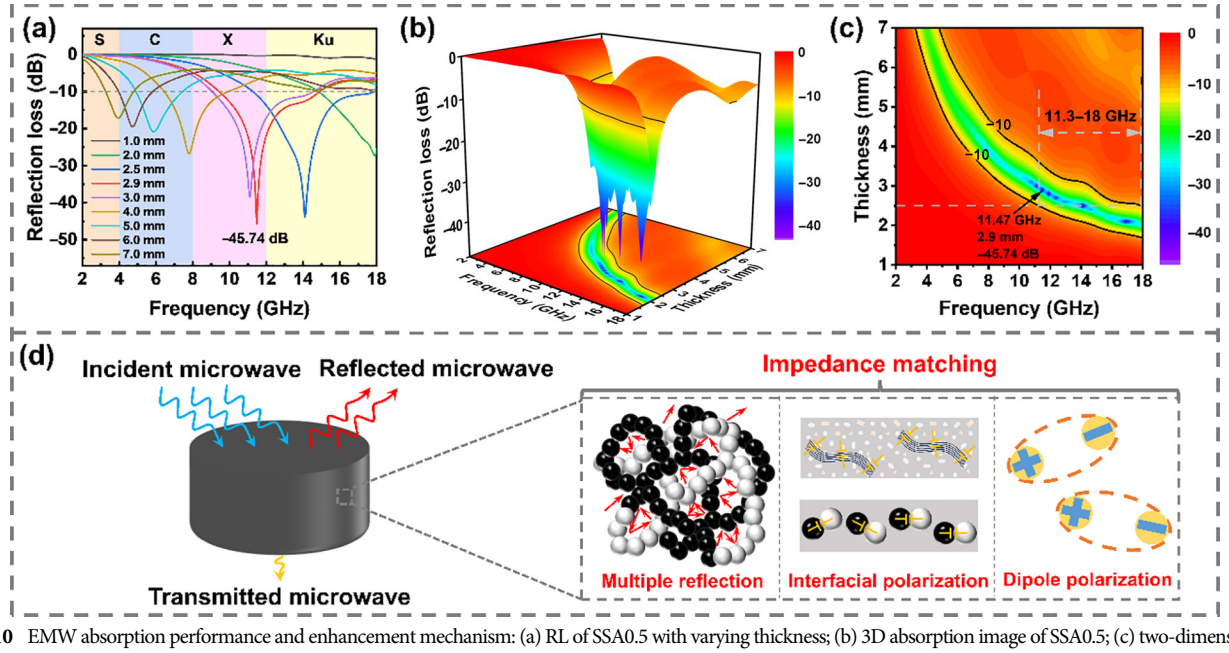

Fig. 10 EMW absorption performance and enhancement mechanism: (a) RL of SSA0.5 with varying thickness; (b) 3D absorption image of SSA0.5; (c) two-dimensional (2D) absorption image of SSA0.5; (d) EMW absorption mechanism of SSA0.5.

SiOC, and free carbon, which have been confirmed through microstructural analyses. The EMW absorption mechanism of the SSA is depicted in Fig. 10(d). The outstanding electromagnetic wave absorption performance of the SiBCN/SiOC composite ceramic aerogel prepared in this work was attributed to the synergistic effect of the constructed multilevel pore structure and multiphase components. The microporous–mesoporous multilevel pore structure of the composite aerogel significantly extended the electromagnetic wave propagation path through multiple reflections and scatters, which effectively enhanced electromagnetic wave absorption [53,54]. Interfacial polarization, also known as space charge polarization, is essentially a phenomenon of charge accumulation that occurs at the interfaces of different phases and components within heterogeneous composite materials [55,56]. For the SiBCN/SiOC composite aerogel, interfacial polarization stemmed from three main interfaces: the interface between the graphitic carbon and the amorphous SiBCN or SiOC matrix, the contact interface between neighboring nanoparticles, and the interface between the aerogel particles and their pores. Interfacial polarization was one of the primary reasons for electromagnetic wave absorption of the SiBCN/SiOC composite aerogels. The dipole polarization caused by the significant differences in electronegativity among Si, B, C, N, and O also contributed to polarization loss [32,57]. Meanwhile, the numerous defects existing under the high specific surface area further increased the polarization sites [58], while the porous structure itself effectively regulated the overall dielectric constant, optimized impedance matching, and ensured high incidence and dissipation of electromagnetic waves.

To study the thermal stability of the SA and SSA0.5, two samples were heat treated at 1600 °C for 60 min in argon. The microstructures of the SA and SSA0.5 samples after heat treatment are shown in Fig. 11. A large number of SiC nanowires were observed within the heat-treated SA sample, while the SSA0.5 sample maintained the original aerogel structure without any SiC nanowires. The density, thermal insulation performance, and mechanical properties of the aerogels after heat treatment were further measured and compared with those of the as-prepared aerogels (Table 2). After heat treatment at 1600 °C, the aerogels still maintained their original bulk shape without any cracks. The linear shrinkage rate of the sample after heat treatment was only approximately 10%, and the density of the heat-treated aerogels remained at 0.08–0.1 g·cm^{-3}, all slightly lower than the density of the as-prepared aerogel. After heat treatment at 1600 °C, the thermal conductivity was basically equal to that of the prepared aerogel, as shown in Table 2. These results indicated that SSA0.5 had good thermal stability under treatment at 1600 °C in argon.

The XRD characterization of the SA and SSA0.5 after heat treatment in argon at 1600 °C for 60 min is shown in Fig. 12(a).

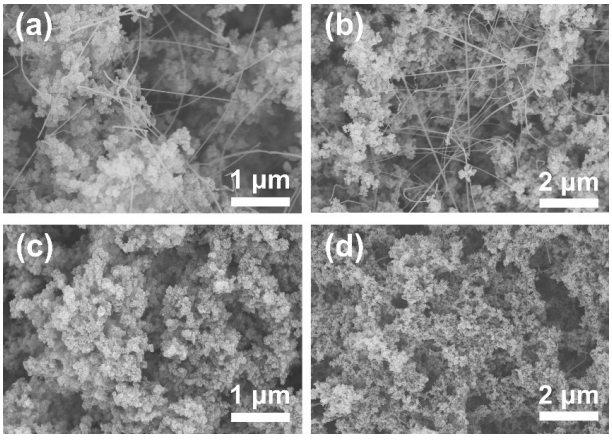

Fig. 11 SEM images of aerogel after thermal treatment at 1600 °C for 60 min in argon: (a, b) SA sample; (c, d) SSA0.5 sample.

Many obvious crystalline peaks appeared in the SA after heat treatment at 1600 °C. These peaks indicated that crystalline phases precipitated in the aerogel. Among them, the crystal diffraction peaks detected at 2θ = 71.8°, 60.0°, and 35.6° corresponded to the diffraction peaks of (311), (220), and (111) of β-SiC (JCPDS 29-1129), respectively. Weak crystal peaks of SiC also appeared after SSA0.5 was heat treated at 1600 °C, but their intensity was significantly lower than that of the SA sample. At the same time, a relatively wide diffraction peak still existed within the 2θ range of 15°–30°, indicating its amorphous state.

The Raman spectra were applied to analyze the state of free carbon in the SA and SSA0.5 samples. As Fig. 12(b) shows, there were two major peaks in the Raman spectra. The D peak (~1350 cm^{-1}) represented the disorder level of the free carbon, and the G peak (~1580 cm^{-1}) reflected the order degree of the free carbon. After heat treatment, the full-width-at-half-maximum (FWHM) of the G peaks decreased, and the position of the G peaks shifted to a higher wavenumber, indicating that the free carbon in the SA and SSA0.5 both underwent the graphitization process. However, the size of the sp^2-carbon clusters in SSA0.5 was smaller than that in SA (Table S1 in the ESM), which illustrated that the free carbon in SSA0.5 was further consumed and that the growth of free carbon in SSA0.5 was inhibited [59]. XPS spectra were used to compare the chemical bonding of the SSA0.5 and SA

Table 2 Density, linear shrinkage, and thermal conductivity of SA and SSA0.5 after thermal treatment at 1600 °C for 60 min in argon

Sample	Atmosphere	Temperature (°C)	Time (min)	Linear shrinkage (%)	Density (g·cm^{-3})	Thermal conductivity (W·m^{-1}·K^{-1})
SA	—	—	—	—	0.117	0.044±0.001
SSA0.5	—	—	—	—	0.135	0.046±0.002
SA	Ar	1600	60	10.3	0.081	0.048±0.001
SSA0.5	Ar	1600	60	9.9	0.095	0.052±0.003

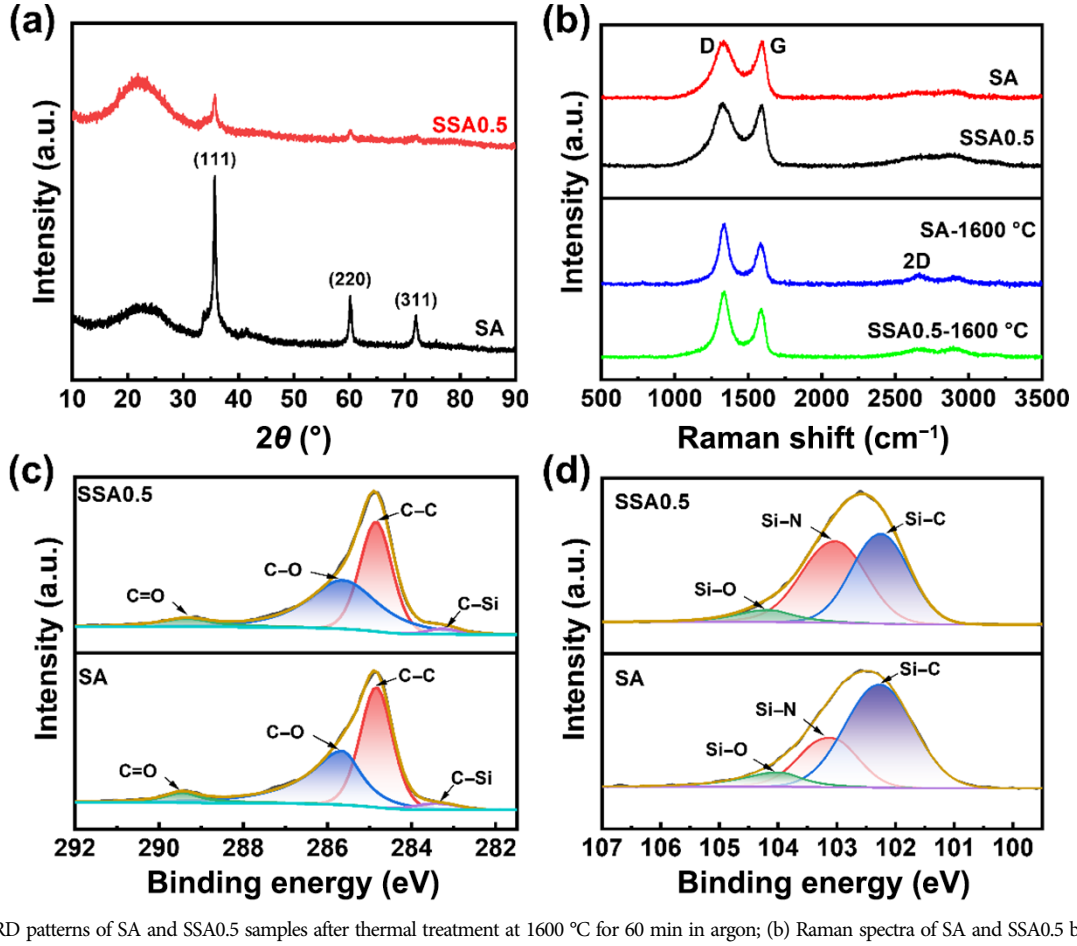

Fig. 12 (a) XRD patterns of SA and SSA0.5 samples after thermal treatment at 1600 °C for 60 min in argon; (b) Raman spectra of SA and SSA0.5 before and after thermal treatment at 1600 °C; XPS spectra of (c) C 1s and (d) Si 2p of SSA0.5 and SA samples after thermal treatment at 1600 °C for 60 min in argon.

after thermal treatment at 1600 °C. The C 1s XPS spectra (Fig. 12(c)) showed that the C–C bond at 284.8 eV, C–O bond at 285.6 eV, and C–Si bond at 283.3 eV were the main structures in the aerogels [60]. There were three major peaks in the Si 2p XPS spectra (Fig. 12(d)), including the Si–O bond at 104 eV, Si–N bond at 103.1 eV, and Si–C bond at 102.2 eV, and the Si–C peak in SA was much higher than that in SSA0.5 [61], indicating that more SiC chemical bonds were formed in the SA sample.

The evolution of chemical bonds in SA and SSA0.5 samples after heat treatment was also revealed by XPS analysis, and the results are shown in Fig. 12, Fig. S4, and Tables S2 and S3 in the ESM. For both aerogels, the content of all the oxygen-containing chemical bonds decreased except the C=O and C–O bonds, which were related to the release of SiO, B_2O_3, and oxynitride at 1600 °C. The C=O bond was attributed to the adsorbed CO_2 from the air during the test. Due to the low oxygen partial pressure in an argon atmosphere, SiO was formed, released to the pores in aerogels, and partly reacted with the free carbon, finally causing an increase in the content of C–O and C–Si bonds (Table S2 in the ESM). Compared with the SA sample, the increase in the C–O bond and the decrease in the C–C bond in the SSA were greater, and the content of the C–Si bond in SSAs was lower. These results indicated that the oxygen in SiOC reacted with the free carbon, thereby preventing the precipitation of SiC nanowires and finally maintaining the original aerogel structure of SSAs at 1600 °C.

As summarized in Table 3, the SiBCN/SiOC composite aerogel prepared by the *in situ* introduction of PHMS via a silicon–hydrogen addition reaction during the solvothermal process demonstrated integrated multifunctional properties (efficient electromagnetic wave absorption, robust mechanical strength, excellent high-temperature stability, and superior thermal insulation performance). The higher number of hydrosilylation sites in PHMS endowed the precursor gel network with an increased crosslinking density, which subsequently resulted in a robust skeleton of the SiBCN/SiOC composite aerogel. The *in situ* introduction of SiOC not only effectively optimized the impedance matching of the composite but also created abundant heterogeneous interfaces among the amorphous matrix and free carbon, which significantly enhanced the electromagnetic wave absorption of the composite aerogel. Moreover, at an elevated temperature of 1600 °C, the *in situ* reaction between SiOC and free carbon effectively suppressed the formation of SiC nanowires, thus enhancing the high-temperature structural stability of the SiBCN/SiOC composite aerogel.

Table 3 Performance comparison between SiBCN/SiOC composite aerogel in this work and similar ceramic aerogels reported in recent literature

SiBCN related aerogel	Mechanical strength (MPa)	Thermal conductivity ($W \cdot m^{-1} \cdot K^{-1}$)	Density ($g \cdot cm^{-3}$)	RL_{min} (dB)	EAB (GHz)	Thickness (mm)	Temperature resistance (°C)	Ref.
SiBCN aerogels	—	—	—	−29.29	3.15	2.2	1400	[62]
SiOC aerogels	1.010	0.070	0.180	—	—		—	[63]
SiCN aerogels	—	0.046	0.190	—	—		1500	[64]
SiOCN aerogels	—	0.035	0.210	−31.60	3.85	1.2	—	[65]
SiBCN/SiC/C aerogel	0.480	0.049	0.116	−45.70	3.80	2.8	—	[26]
SiOC fiber aerogel	0.167	0.044	0.128	—	—		—	[66]
SiBCN/SiC_{nw} aerogel	—	0.052	0.142	−50.10	6.40	2.0	—	[21]
rGO/SiBCN aerogel	0.056	0.057	0.070	—	—		1200	[61]
This work	0.510	0.046	0.135	−43.89	6.70	2.5	1600	

4 Conclusions

In conclusion, a new type of SiBCN/SiOC amorphous ceramic aerogel was successfully synthesized through solvothermal synthesis, freeze-drying, and heat treatment processes. The content of SiOC in the composite aerogel could be adjusted by changing the initial ratio of PSNB and PHMS, thereby regulating the morphology and properties of the resulting composite aerogel. The density of the SSA sample was 0.135 $g \cdot cm^{-3}$, and the thermal conductivity was 0.046 $W \cdot m^{-1} \cdot K^{-1}$. Meanwhile, SSAs exhibited a compressive strength of 0.51 MPa, which was 260% higher than that of SAs (0.14 MPa) due to the more stable three-dimensional network. The microwave absorption performance of the composite aerogel was dramatically improved with an RL value of −43.89 dB and an EAB_{max} value of 6.7 GHz at a thickness of 2.5 mm, which was attributed to the optimized impedance matching and enhanced interfacial polarization, as well as the multireflection effect. In addition, the SiBCN/SiOC composite aerogel exhibited excellent high-temperature structural stability up to 1600 °C. Overall, due to its lightweight structure, robust mechanical strength, excellent microwave absorption, outstanding thermal insulation performance, and high-temperature stability, the SSA shows broad application prospects in the aerospace and high-temperature electromagnetic stealth fields.

Acknowledgements

This work was financially supported by the National Key R&D Program of China (No. 2023YFB3711200) and the National Natural Science Foundation of China (No. 52572081).

Author contributions

Jiale Wang: experiments, data processing and analysis, and manuscript writing. Yifan Li: experiments, data processing and analysis. Jingrui Cao: data processing and analysis. Yixin Zhang: writing – review and editing. Boxuan Feng: experiments, data processing and analysis. Anran Guo: inspection and proofreading. Liwen Yan: writing – review and editing, supervision, and funding acquisition. Ping Hu: writing – review and editing, methodology, and conceptualization. Jiachen Liu: supervision, resources, funding acquisition, methodology, and conceptualization.

Availability of data and materials

The data that support the findings of this study are available from the corresponding author upon reasonable request.

Competing interests

The authors have no competing interests to declare that are relevant to the content of this article.

Electronic Supplementary Material

Supplementary material is available in the online version of this article at https://doi.org/10.26599/JAC.2026.9221256.

References

[1] Liang J, Zhu SY, Chen DW, *et al.* Dual built-in electric field engineering in heterostructure nickel–cobalt bimetallic composites for boosted electromagnetic energy dissipation. *Adv Powder Mater* 2025, **4**: 100344.

[2] Su L, Jia SH, Ren JQ, *et al.* Strong yet flexible ceramic aerogel. *Nat Commun* 2023, **14**: 7057.

[3] Li JQ, Zhang L, Pang YC, *et al.* Polyimide composite aerogels towards highly efficient microwave absorption and thermal insulation. *Compos Part A—Appl S* 2022, **161**: 107112.

[4] Lee H, Lee D, Cho J, *et al.* Super-insulating, flame-retardant, and flexible poly(dimethylsiloxane) composites based on silica aerogel. *Compos Part A—Appl S* 2019, **123**: 108–113.

[5] Luo JW, Wang Y, Qu ZJ, *et al.* Lightweight and robust cobalt ferrite/carbon nanotubes/waterborne polyurethane hybrid aerogels for efficient microwave absorption and thermal insulation. *J Mater Chem C* 2021, **9**: 12201–12212.

[6] Si Y, Wang XQ, Dou LY, *et al.* Ultralight and fire-resistant ceramic nanofibrous aerogels with temperature-invariant superelasticity. *Sci Adv* 2018, **4**: eaas8925.

[7] Hou XB, Zhang RB, Fang DN. An ultralight silica-modified ZrO_2–SiO_2 aerogel composite with ultra-low thermal conductivity and enhanced mechanical strength. *Scripta Mater* 2018, **143**: 113–116.

[8] Xu L, Zhu WX, Chen ZW, *et al.* Double-network MK resin-modified silica aerogels for high-temperature thermal insulation. *ACS Appl Mater Inter* 2023, **15**: 44238–44247.

[9] Liu BX, Gao M, Liu XC, *et al.* Thermally stable nanoporous ZrO_2/SiO_2 hybrid aerogels for thermal insulation. *ACS Appl Nano Mater* 2019, **2**: 7299–7310.

[10] Chao XY, Yuan WH, Shi QY, *et al.* Improvement of thermal stability of zirconia aerogel by addition of yttrium. *J Sol-Gel Sci Techn* 2016, **80**: 667–674.

[11] Chang XY, Cheng XT, Zhang H, *et al.* Superelastic carbon aerogels: An emerging material for advanced thermal protection in extreme environments. *Adv Funct Mater* 2023, **33**: 2215168.

[12] Wu XD, Shao GF, Shen XD, *et al.* Evolution of the novel C/SiO_2/SiC ternary aerogel with high specific surface area and improved oxidation resistance. *Chem Eng J* 2017, **330**: 1022–1034.

[13] Song LM, Fan BB, Chen YQ, *et al.* Ultralight and hyperelastic SiC nanofiber aerogel spring for personal thermal energy regulation. *J Adv Ceram* 2022, **11**: 1235–1248.

[14] Chen SL, Wang L, He G, *et al.* Microstructure and properties of porous Si_3N_4 ceramics by gelcasting-self-propagating high-temperature synthesis (SHS). *J Adv Ceram* 2022, **11**: 172–183.

[15] Han L, Li XJ, Li FL, *et al. In-situ* preparation of SiC reinforced Si_3N_4 ceramics aerogels by foam-gelcasting method. *Ceram Int* 2022, **48**: 1166–1172.

[16] Su L, Li MZ, Wang HJ, *et al.* Resilient Si_3N_4 nanobelt aerogel as fire-resistant and electromagnetic wave-transparent thermal insulator. *ACS Appl Mater Inter* 2019, **11**: 15795–15803.

[17] Yuan KK, Han DY, Liang JF, *et al.* Microwave induced *in-situ* formation of SiC nanowires on SiCNO ceramic aerogels with excellent electromagnetic wave absorption performance. *J Adv Ceram* 2021, **10**: 1140–1151.

[18] Nguyen VL, Zera E, Perolo A, *et al.* Synthesis and characterization of polymer-derived SiCN aerogel. *J Eur Ceram Soc* 2015, **35**: 3295–3302.

[19] Zhou Q, Zhang Y, Li YK, *et al.* Multi-scale GNS/SiC@SiBCN hybrid aerogels with tailorable electromagnetic wave absorption via hierarchical design. *Carbon* 2026, **246**: 120911.

[20] Zhu WX, Xia XH, Su D, *et al.* Carbon foam reinforced SiBCN ceramic aerogel with multifunctional performances. *J Am Ceram Soc* 2025, **108**: e20536.

[21] Jiang JP, Yan LW, Xue YJ, *et al.* Lightweight and thermally insulating polymer-derived SiBCN/SiC_{nw} ceramic aerogel with enhanced electromagnetic wave absorbing performance. *Chem Eng J* 2024, **482**: 148878.

[22] Hu ZF, Wang HJ, Su D. *In situ* formation of high-entropy carbide phase in porous SiBCN ceramic for enhanced high-temperature stability. *J Adv Ceram* 2025, **14**: 9221019.

[23] Wang HJ, Hu ZF, Su D. Construction of ZrC@SiC shell–core structure in SiBCN aerogel for enhanced thermal stability and thermal insulation. *Chem Eng J* 2024, **499**: 156158.

[24] Jiang JP, Xue YJ, Li JT, *et al.* Microwave absorption and thermal insulation integrated polymer-derived SiBCN/$SiBCN_{nf}$ ceramic aerogel with enhanced mechanical property. *Ceram Int* 2024, **50**: 41527–41533.

[25] Wang ZQ, Wang SB, Fei H, *et al.* Atomic-scale elucidation of attenuation mechanisms underlying exceptional electromagnetic wave absorption of SiZrBCN ceramic nanocomposites. *J Adv Ceram* 2026, **15**: 9221221.

[26] Jiang JP, Yan LW, Song MJ, *et al.* Thermally insulated C/SiC/SiBCN composite ceramic aerogel with enhanced electromagnetic wave absorption performance. *Ceram Int* 2025, **51**: 17–24.

[27] Jiang JP, Yan LW, Li JT, *et al.* Lightweight, thermally insulating SiBCN/Al_2O_3 ceramic aerogel with enhanced high-temperature resistance and electromagnetic wave absorption performance. *Chem Eng J* 2024, **501**: 157656.

[28] Li W, Li XC, Gong W, *et al.* Construction of multiple heterogeneous interface and its effect on microwave absorption of SiBCN ceramics. *Ceram Int* 2020, **46**: 7823–7832.

[29] Jiang JP, Yan LW, Li JT, *et al.* Lightweight and resilient SiBCNa/mullite/SiC_{nw} composite for thermal insulation and electromagnetic wave absorption. *Ceram Int* 2025, **51**: 2315–2323.

[30] Zhu WX, Wang H, Ji HM, *et al.* Lightweight aerogel-like silicon oxycarbide ceramics with directionally honeycomb-like structure for high temperature environments. *J Eur Ceram Soc* 2024, **44**: 4027–4035.

[31] Qian JJ, Ma DD, Zhou XL, *et al.* Synthesis of SiOC@C ceramic nanospheres with tunable electromagnetic wave absorption performance. *J Adv Ceram* 2024, **13**: 1394–1408.

[32] Yang DD, Dong S, Xin JQ, *et al.* Robust and thermostable C/SiOC composite aerogel for efficient microwave absorption, thermal insulation and flame retardancy. *Chem Eng J* 2023, **469**: 143851.

[33] Wang H, Zhu WX, Sun XL, *et al.* Preparation of aerogel-like SiOC ceramic with honeycomb structure and its high-temperature performance. *J Alloy Compd* 2023, **937**: 168438.

[34] Li J, Guo PL, Hu CL, *et al.* Fabrication of large aerogel-like carbon/carbon composites with excellent load-bearing capacity and thermal-insulating performance at 1800 °C. *ACS Nano* 2022, **16**: 6565–6577.

[35] Tong ZW, Yan BX, Zhang BJ, *et al.* Preparation and textural evolution: From organosilane aerogel to SiOC aerogels. *Ceram Int* 2022, **48**: 5468–5475.

[36] Yang DD, Dong S, Cui TY, *et al.* Multifunctional carbon fiber reinforced C/SiOC aerogel composites for efficient electromagnetic wave absorption, thermal insulation, and flame retardancy. *Small* 2024, **20**: 2308145.

[37] Zhang J, Yin RY, Fan ZH, *et al.* Significantly enhanced mechanical, thermal, and ablative properties of the lightweight carbon fabric/phenol-formaldehyde resin/siloxane aerogels ternary interpenetrating network. *ACS Appl Mater Inter* 2024, **16**: 38520–38530.

[38] Jia XF, Dai BW, Zhu ZX, *et al.* Strong and machinable carbon aerogel monoliths with low thermal conductivity prepared via ambient pressure drying. *Carbon* 2016, **108**: 551–560.

[39] Wang BL, Li GY, Xu L, *et al.* Nanoporous boron nitride aerogel film and its smart composite with phase change materials. *ACS Nano* 2020, **14**: 16590–16599.

[40] Zhu JD, Zhao FX, Peng TP, *et al.* Highly elastic and robust hydroxyapatite nanowires/polyimide composite aerogel with

anisotropic structure for thermal insulation. *Compos Part B—Eng* 2021, **223**: 109081.
[41] Wu C, Chen ZF, Wang F, *et al.* Preparation and characterization of ultralight glass fiber wool/phenolic resin aerogels with a spring-like structure. *Compos Sci Technol* 2019, **179**: 125–133.
[42] Su L, Wang HJ, Niu M, *et al.* Ultralight, recoverable, and high-temperature-resistant SiC nanowire aerogel. *ACS Nano* 2018, **12**: 3103–3111.
[43] Hu FY, Zhang F, Wang XH, *et al.* Ultrabroad band microwave absorption from hierarchical $MoO_3/TiO_2/Mo_2TiC_2T_x$ hybrids via annealing treatment. *J Adv Ceram* 2022, **11**: 1466–1478.
[44] Xu CY, Xiong XH, Du YQ, *et al.* Dual-coupling networks engineering of self-assembled ferromagnetic microspheres with enhanced interfacial polarization and magnetic interaction for microwave absorption. *InfoMat* 2025, **7**: e12645.
[45] Song Y, Yin FX, Zhang CW, *et al.* Three-dimensional ordered mesoporous carbon spheres modified with ultrafine zinc oxide nanoparticles for enhanced microwave absorption properties. *Nano-Micro Lett* 2021, **13**: 76.
[46] Shu RW, Yi X, Yun KL, *et al.* Synthesis of PAN/ZIF-67 derived composite fibers through electrospinning technology with superior Ku-band electromagnetic absorption performance. *Carbon* 2025, **243**: 120531.
[47] Wang ZC, Wei RB, Gu JW, *et al.* Ultralight, highly compressible and fire-retardant graphene aerogel with self-adjustable electromagnetic wave absorption. *Carbon* 2018, **139**: 1126–1135.
[48] Cui ZR, Li XF, Zhang H, *et al.* Tailoring sulfur/nitrogen co-doping configuration in MXene nanoribbon/nanosheet composite for high-performance electromagnetic wave absorption. *J Adv Ceram* 2025, **14**: 9221209.
[49] Dong YY, Zhu XJ, Pan F, *et al.* Implanting $NiCo_2O_4$ equalizer with designable nanostructures in agaric aerogel-derived composites for efficient multiband electromagnetic wave absorption. *Carbon* 2022, **190**: 68–79.
[50] Zhao HB, Cheng JB, Wang YZ. Biomass-derived Co@crystalline carbon@carbon aerogel composite with enhanced thermal stability and strong microwave absorption performance. *J Alloy Compd* 2018, **736**: 71–79.
[51] Yang LY, Yin LH, Hong CQ, *et al.* Strong and thermostable hydrothermal carbon coated 3D needled carbon fiber reinforced silicon–boron carbonitride composites with broadband and tunable high-performance microwave absorption. *J Colloid Interf Sci* 2021, **582**: 270–282.
[52] Lu SR, Xia L, Xu JM, *et al.* Permittivity-regulating strategy enabling superior electromagnetic wave absorption of lithium aluminum silicate/rGO nanocomposites. *ACS Appl Mater Inter* 2019, **11**: 18626–18636.
[53] Zhao B, Yan ZK, Liu LL, *et al.* A liquid-metal-assisted competitive galvanic reaction strategy toward indium/oxide core–shell nanoparticles with enhanced microwave absorption. *Adv Funct Mater* 2024, **34**: 2314008.
[54] Zhao B, Du YQ, Lv HL, *et al.* Liquid-metal-assisted programmed galvanic engineering of core–shell nanohybrids for microwave absorption. *Adv Funct Mater* 2023, **33**: 2302172.
[55] Ding X, Zhao XQ, Zhang JX, *et al.* Fabrication of chitosan/MIL-88A derived nitrogen-doped carbon/ferroferric oxide/carbon composite aerogels for electromagnetic wave absorption and thermal insulation. *Carbon* 2026, **246**: 120957.
[56] Yun KL, Shu RW, Yi X, *et al.* Nitrogen-doped reduced graphene oxide/copper ferrite@polypyrrole composite aerogels for broadband electromagnetic wave absorption. *Chem Eng J* 2025, **518**: 164748.
[57] Cui RP, Li Y, Zhang XF, *et al.* Controlled deintercalation of graphene /organic superlattices with dense atomic-scale steric Schottky heterojunctions for extreme microwave absorption. *Nat Commun* 2025, **16**: 5804.
[58] Cui RP, Duan ZW, Li Y, *et al.* High-temperature oxide ceramic microwave absorber enabled by thermionic migration mediated by electron delocalization. *Nat Commun* 2025, **16**: 9179.
[59] Chowdhury MAR, Wang KW, Jia YJ, *et al.* Semiconductor-conductor transition of pristine polymer-derived ceramics SiC pyrolyzed at temperature range from 1200 °C to 1800 °C. *J Am Ceram Soc* 2020, **103**: 2630–2642.
[60] Li YF, Yan LW, Song MJ, *et al.* Integration of thermal protection and structural health monitoring for carbon fiber reinforced SiBCN composites with SiC coating enhanced interfacial performance. *Ceram Int* 2023, **49**: 21678–21687.
[61] Wang HJ, Chen ZW, Su D. Lightweight and large-scale rGO reinforced SiBCN aerogels with hierarchical cellular structures exposed to high-temperature environments. *J Mater Sci Technol* 2024, **179**: 145–154.
[62] Wang Y, Luo CJ, Wu YF, *et al.* High temperature stable, amorphous SiBCN microwave absorption ceramics with tunable carbon structures derived from divinylbenzene crosslinked hyperbranched polyborosilazane. *Carbon* 2023, **213**: 118189.
[63] Wang RB, Xu WL, Huang Z, *et al.* Facile preparation of SiOC ceramic aerogels based on vinyl-hydrogen polysiloxane. *Mater Today Commun* 2025, **49**: 113967.
[64] Wang W, Pang L, Jiang M, *et al.* Enhancing the thermal insulation properties of polymer-derived SiCN(O) ceramic aerogels with a polysilazane-precursor design. *Ceram Int* 2023, **49**: 15829–15841.
[65] Wang RY, Wang F, Zhu YP, *et al.* Polysilazane hybrid phenolic resin ceramic aerogels with excellent electromagnetic wave absorption performance. *J Am Ceram Soc* 2024, **107**: 1170–1184.
[66] Dong X, Liu RL, Dong W, *et al.* Fabrication and properties of lightweight SiOC fiber-based assembly aerogels with hierarchical pore structure. *Ceram Int* 2018, **44**: 22760–22766.